Observed Dependence of Outgoing Longwave Radiation on Sea Surface Temperature and Moisture

A. RAVAL AND A. H. OORT

Geophysical Fluid Dynamics Laboratory/NOAA, Princeton, New Jersey

V. RAMASWAMY

AOS Program, Princeton University, Princeton, New Jersey

ABSTRACT

The authors have empirically examined the dependence of the outgoing longwave radiation (OLR) on sea surface temperature (T_s), precipitable water (W), and height-mean relative humidity ($\overline{RH}$). The OLR is obtained from 4 yr of data from the Earth Radiation Budget Experiment (ERBE), while T_s, W, and $\overline{RH}$ are obtained from objective analyses of rawinsonde and ship data. It is found that in the midlatitudes, the surface temperature explains over 80% of the variability in the clear-sky OLR (F_{cs}) and almost half of the variability in the total OLR (F_{tot}). It fails badly in the tropics and subtropics, however, where T_s explains only about 20% of the variability in F_{cs}, and is largely decoupled from F_{tot}. The two-dimensional contour plot of the OLR binned with respect to T_s and $\overline{RH}$ is marked by distinct changes in the gradient that are consistent with inferences from earlier investigations. For low values of T_s ($<10°C$), the OLR depends mainly on T_s. For values of T_s above 10°C, the OLR depends increasingly on $\overline{RH}$. Specifically, in the tropics ($T_s \sim 25°C$), the total and clear-sky OLR depend significantly on both T_s and $\overline{RH}$. The well-known drop in OLR in the tropics with increasing T_s correlates directly to an increase in $\overline{RH}$, and not to changes in T_s. The authors suggest that the observed dependence of the OLR on T_s and $\overline{RH}$ be a minimum performance standard for climate models. This approach is illustrated by comparing the observed dependence with the results of a radiative transfer model and an R15 general circulation model, and by discussing the strengths and limitations of using $\overline{RH}$ to parameterize the OLR.

1. Introduction

The possibility of human-induced climate change is challenging researchers to understand better the sensitivity and stability of the earth's present climate. The outgoing longwave radiation (OLR) is an important component of the earth's total energy budget. Consequently, a great number of studies have attempted to relate the OLR to observed climate variables. The surface temperature (T_s) is commonly used for this purpose, because it is important in its own right in the state of the climate, and also because T_s determines the emission of longwave radiation at the surface, which contributes heavily to the magnitude of the OLR (Budyko 1968; Sellers 1969; Warren and Schneider 1979; North et al. 1981; Raval and Ramanathan 1989).

A number of studies, however, have shown that T_s alone cannot fully represent the OLR over the full range of the climate system (Budyko 1969; Cess 1976; Stephenson-Graves 1982; Warren and Thompson 1983;

Short et al. 1984; Kubota 1989). Most of these studies find that, to explain the behavior of the OLR more fully, one needs to invoke additional parameters such as cloudiness, cloud-top height, moisture, lapse rate, or surface convergence (a proxy for deep convection). In fact, in regions of deep convection, the cloud-top height, more than any other parameter, controls the OLR.

The chief objective of this paper is to consider the OLR as a function of two climate variables, the surface temperature (T_s) and the height-mean tropospheric relative humidity ($\overline{RH}$) (Thompson and Warren 1982). We obtain the OLR data for this study from the Earth Radiation Budget Experiment (ERBE), which provides information on the "total" flux (F_{tot}) as well as the "clear-sky" flux (F_{cs}) that one would obtain in a hypothetical cloud-free case (Barkstrom 1984; Ramanathan et al. 1989). Although deep convection and its attendant clouds have a significant impact on the OLR of the tropical atmosphere, our study is primarily geared toward the observed dependence of the clear-sky OLR. The surface temperature and vertical profiles of humidity are derived from objective

analyses of rawinsonde and ship data [Oort (1983), updated]. We emphasize that T_s and $\overline{RH}$ are not the only possible pair of parameters. Instead of $\overline{RH}$, for example, one could use the column-integrated water vapor (W). But because the total column moisture is tied strongly to the surface temperature (section 3, below, finds correlations of +0.65 to +0.8), T_s and W are not independent, and W adds little information.

We suggest that the functional dependence of the observed OLR on T_s and $\overline{RH}$ (or a similar grouping of variables) should be used as a minimum performance standard for climate models. A model that cannot reproduce this basic structure should not, perhaps, be trusted on even more subtle predictions. We compare our inferred dependence of the observed OLR with that obtained from a two-parameter model and from a GCM.

In section 2 we review the data sources and the operational definitions of the variables used in this paper. In section 3 we show global correlations between the variables. While T_s correlates well with the OLR in the midlatitudes, it represents the total and clear-sky OLR poorly in the subtropics and the tropics. In section 4a we depict, with two-dimensional binned plots, the observed dependence of the OLR on T_s and W or $\overline{RH}$, as obtained from ERBE and gridded rawinsonde data. As an illustration of the use of these plots, we also consider (in section 4b) a simple two-parameter model (Thompson and Warren 1982), which is a third-order polynomial fit to the output of a more detailed radiation transfer algorithm, and (in section 4c) a general circulation model (Wetherald et al. 1991) that simulates many aspects of the climate. Finally, in section 5 we summarize and discuss the results of the paper.

2. Data sources and data reduction

a. ERBE total and clear-sky OLR data

The Earth Radiation Budget Experiment satellite system, which began operating in 1984, has been providing measurements of the energy fluxes at the top of the atmosphere in both the longwave and shortwave radiation spectral regions. A unique feature of ERBE is that in the flux retrieval and binning algorithms, pixels that are entirely free of clouds are averaged separately to yield a "clear-sky" representation of both longwave and shortwave fields. The clear-sky version of a field is a hypothetical map of the radiation field as though all clouds were instantaneously removed.

We use the ERBE monthly averages of the OLR, binned on a 2.5° × 2.5° grid. We only use data over oceans; this lets us avoid the greater diurnal variations of the surface temperature over land and the uneven longwave emissivity of land surfaces. The data used in this paper span 47 months, from February 1985 through December 1988.

The accuracy of the ERBE data varies according to the parameter viewed and the time and space resolution. A "standard" estimate of ERBE OLR error is about 5 W m^{-2} for the monthly average value at a single grid box. Averages in space or time are also assigned an error of about 5 W m^{-2} (Barkstrom et al. 1989).

b. Meteorological data

The meteorological data used in this study come from in situ measurements. Ships and island stations in the Comprehensive Oceanic and Atmospheric Data Set (COADS) network provided sea surface temperature (T_s) readings. A global network of more than 800 rawinsonde stations provided upper-air balloon soundings of humidity and temperature at standard pressure levels [Oort (1983), updated]. The measurements were objectively analyzed onto the same 2.5° × 2.5° grid as the ERBE data and were averaged monthly. The objective analysis scheme is described in detail in Oort (1983). The rawinsonde stations that, over the 47-month period, reported 10 or more months (with at least 10 daily soundings in each month) are shown in Fig. 1a by small plus signs. Some grid points, especially in the equatorial Pacific and the southern Pacific (~50°S), are more than 2000 km away from the nearest island or coastal station (shown as the shaded areas in Fig. 1a). Our confidence in the analysis is low at those points, and the data there are not included in any of the global or regional correlation statistics in this paper. In all comparisons with ERBE data we match the ERBE time period—February 1985 through December 1988, but in plots of annual average values (Figs. 1a and 1c) we use a full 4 years from January 1985 through December 1988.

The column-integrated water vapor (W) was obtained by vertically integrating the gridded observations of specific humidity between the surface and 250 mb. Figure 1a shows the annual average distribution of W. The main feature of this plot is the steady increase of W from the poles to the equator. A secondary feature is the maximum ($W > 50$ kg m^{-2}) in the western equatorial Pacific "warm pool." This can be attributed to the Clausius–Clapeyron effect, which specifies that the saturation vapor pressure increases exponentially with T (Raval and Ramanathan 1989; Stephens 1990).

To check on the overall validity of the analyzed W, we compared it with satellite-based measurements from the Special Sensor Microwave/Imager (SSM/I) (Stephens et al. 1993; Greenwald et al. 1993). We should note here that in our analysis scheme of the rawinsonde data we used the zonal mean station values as a first guess; this first-guess value does not get changed in data-sparse regions and may create too much zonal symmetry in the field. Figure 1b shows the difference between the annual averages of the rawinsonde analyzed W and the SSM/I W for the normal, non–El
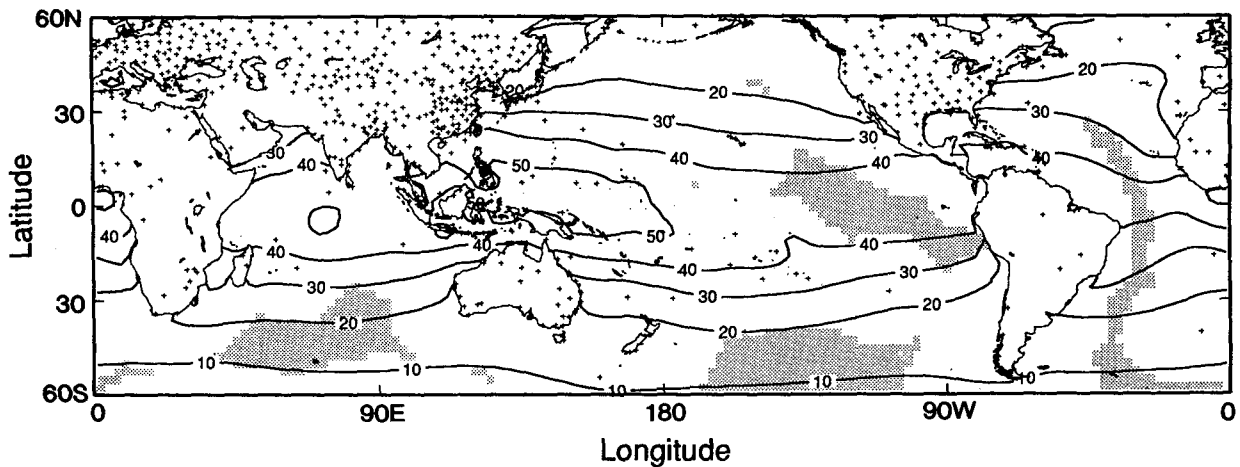
FIG. 1a. Global map of annual average column-integrated precipitable water W (kg m^{-2}), based on data from the rawinsonde network for the period January 1985–December 1988. Shaded areas are more than 2000 km from the nearest rawinsonde station, where the rawinsonde analyses cannot be trusted. Plus signs indicate the location of rawinsonde stations with at least 10 months (usually 30 or more) of good data during the period studied.

Niño year 1989. The two sources agree fairly well (to within 5 kg m^{-2}) poleward of 10°N and 30°S. The areas of greatest discrepancy are found in the rawinsonde-sparse area (shaded area in Fig. 1a) of the eastern tropical Pacific (centered near 15°S, 100°W), where the greatest W anomalies from the zonal mean are also found. In fact, during strong La Niña episodes (cold sea surface temperatures), we find that the zonal anomalies are strongest, and thus the discrepancies in the eastern tropical Pacific are the worst (up to 20 kg m^{-2}); whereas during El Niño events (warm sea surface temperatures) the zonal anomalies are weakened, and thus the discrepancies are smallest (up to about 10 kg m^{-2}). There are also significant discrepancies, up to about 5 kg m^{-2} in the rest of the equatorial Pacific, the eastern equatorial Atlantic, and the Indian Ocean just west of Australia. In most of these areas the annual average rawinsonde W is larger by 5–10 kg m^{-2} than the SSM/I measurements. The difference map provides a good measure of the locations of the largest uncertainties in our humidity analyses.

The height-mean relative humidity ($\overline{RH}$) was obtained following the definition of Thompson and Warren (1982). They define it as the average relative humidity from the surface to a constant height H:

$$\overline{RH} = \frac{1}{H} \int_0^H RH(z)\,dz, \qquad (1)$$

where H is set equal to 12 km. Note that this definition of $\overline{RH}$ differs from the traditional definition of mean relative humidity, which weights each layer in the atmosphere with its mass, or pressure thickness, rather than its height. Although $\overline{RH}$ is merely one empirical choice for a moisture parameter, Thompson and War-

ren find that it forms a more robust and stable predictor of OLR fluxes than the traditional RH. Specifically, they find that if the vertical distribution of the water vapor is altered by up to 20%, provided $\overline{RH}$ is held fixed, then the computed OLR changes by less than 1 W m^{-2}. In the upper troposphere, a given vertical distance contains much less mass than it would lower down, and so perhaps $\overline{RH}$ performs better as a predictor for the OLR because it preferentially weights upper-tropospheric specific humidity variations (Thompson and Warren 1982).

We calculate $\overline{RH}$ from the meteorological observations by averaging from the surface level up to the 10-km height, using Eq. (1), with $H = 10$ km. Figure 1c shows the annual average distribution of $\overline{RH}$. Unlike W, $\overline{RH}$ does not increase as a rule with T_s, but instead seems to follow the large-scale patterns of upward motion and subsidence. For example, both subtropical belts (15°–45° lat), where subsidence prevails, have lower values of $\overline{RH}$ as compared to the regions of generally upward motions in the tropics and midlatitudes. Extremely low values register in the "oceanic deserts," such as off the west coasts of North and South America, while high values register in the equatorial Pacific warm pool and at high latitudes.

3. Analysis of correlations

Here we present some observed correlations between OLR, T_s, and moisture (in the form of both column-integrated water vapor and height-mean relative humidity). We begin by examining the connection between the clear-sky OLR and T_s over the course of the annual cycle. Next, by creating maps of the correlations, we examine how the correlations depend criti-
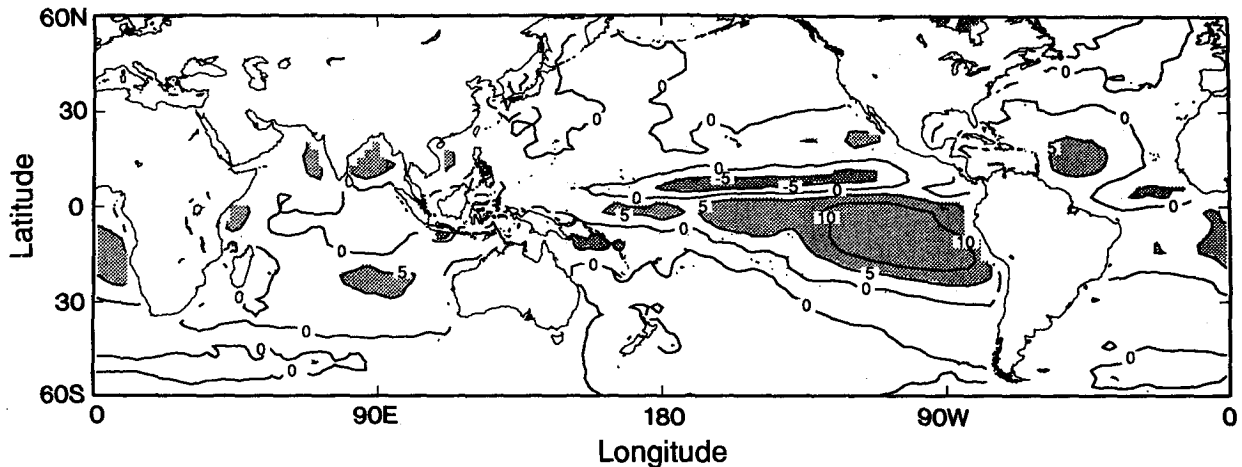
FIG. 1b. Global map of the difference (rawinsonde − SSM/I) in precipitable water W for a typical non–El Niño year (1989) between our analyses using the rawinsonde stations and the Special Sensor Microwave/Imager (SSM/I) analyses (kg m^{-2}). Outside the tropics, differences are less than 5 kg m^{-2}. The most substantial differences (above 10 kg m^{-2}) are found in the eastern tropical South Pacific Ocean, where the zonal anomalies in W are largest, according to the SSM/I analyses, and where the rawinsonde network is very sparse (see text for further discussion).

cally on the latitude of the region. Finally, we show correlation matrices that present these regional differences succinctly, and point to T_s and $\overline{RH}$ as a good set of variables for parameterizing the OLR.

a. Annual cycle at individual locations

Figure 2 shows a scatterplot of F_{cs} versus T_s over all the months at three different grid points chosen to be representative of the eastern subtropical Pacific, the midlatitude Pacific, and the western equatorial Pacific. Mainly, the annual cycle drives the variability at each region. Since the seasonal range of the sea surface temperature at each grid point is greater than the typical

interannual variability (Gutzler and Wood 1990) (except in the eastern tropical Pacific), year-to-year variations probably affect only the vertical spread of the data points, and not the overall slope. In the eastern Pacific and in the midlatitudes, F_{cs} is positively linked to T_s with a slope of 1.8–2.4 W m^{-2} K^{-1} ($r \sim 0.85$). However, in the western Pacific, it is negatively linked (i.e., it downturns) with a slope of -1.0 ± 0.3 W m^{-2} K^{-1} ($r \sim -0.44$). Thus a single linear, monotonic fit that tries to cover all regions will prove inadequate.

b. Latitude–longitude map of annual cycle

Raval and Ramanathan (1989) pooled clear-sky fluxes over all ocean regions in 1 month (April 1985)
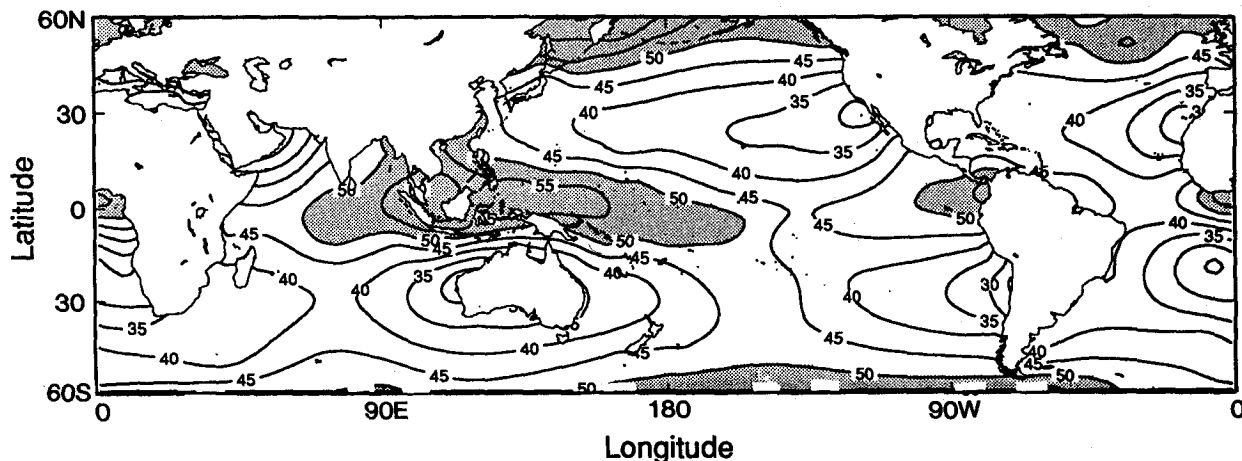

FIG. 1c. Global map of the annual average (height weighted) vertical-mean relative humidity $\overline{RH}$ (%) (see text), based on the rawinsonde network for the period January 1985–December 1988.
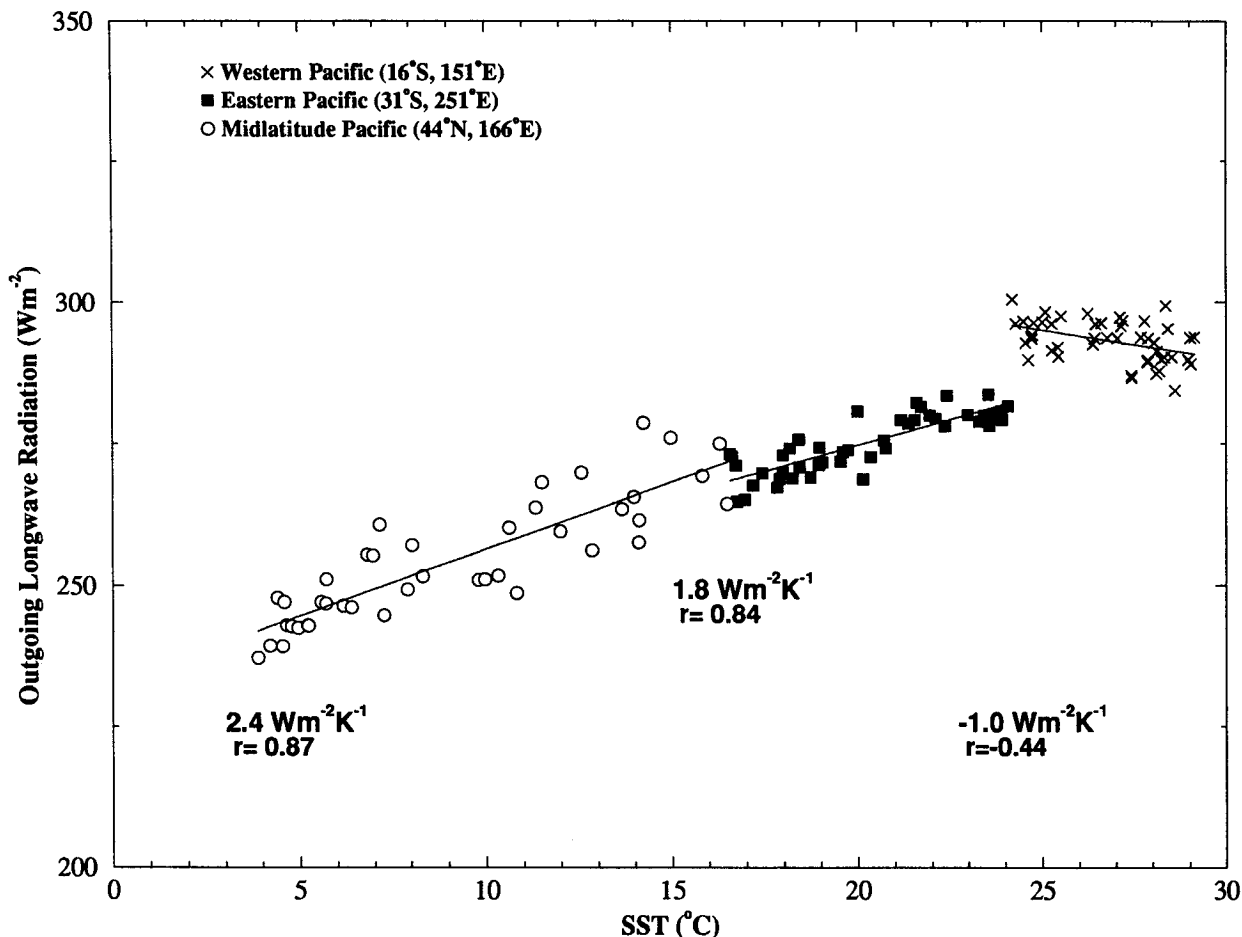
FIG. 2. The monthly mean clear-sky outgoing longwave radiation F_{cs} observed by ERBE and plotted as a function of sea surface temperature T_s for the period February 1985–December 1988, at three separate locations in the western Pacific (cross), eastern Pacific (solid square), and midlatitude Pacific (open circle). Note the change in sign of the slope above 25°C.

to calculate a single slope value for their "clear-sky greenhouse effect," g, defined in the following equation:

$$F_{cs} = (1 - g(T_s))\sigma T_s^4. \qquad (2)$$

The slope of g with respect to T_s is 3.42×10^{-3} K^{-1}; cast in terms of F_{cs} at the global mean temperature of 15°C, this yields a slope of 2.3 W m^{-2} K^{-1}.

Here, we calculate local slopes for the observed F_{cs} and T_s, and plot the slopes on a map in Fig. 3a. The value at each location on the "slope map" represents the linear regression through the 47 months of data. We repeat this procedure for the total OLR in Fig. 3b.

The chief feature of Fig. 3a (clear-sky OLR) is the large area of negative slopes throughout the tropics; we will shortly explore its statistical significance. Another feature is that the slope in the midlatitude oceans is uniformly positive, with a value around 2–3 W m^{-2} K^{-1}. For comparison, Fig. 3b (for total OLR) has a similar large expanse of negative slopes, but with even

more extreme, negative values. A likely cause is the high clouds formed in deep convection that can accompany surface temperatures above a critical value (Graham and Barnett 1987). Both plots have an area with positive slopes in the tropical Indian Ocean, west of Sumatra. We do not know the reason for this anomaly.

Figure 4a shows the local linear correlation between F_{cs} and T_s, as an estimate of the significance of the slopes presented in Fig. 3a. Values of $|r| > +0.4$ [95% significant for 20 degrees of freedom; see Spiegel (1961)] are shaded to emphasize the regions of strongest positive and negative correlation. The chief feature of this plot is the change in sign of r from the midlatitudes to the tropics. The positive sign in the midlatitudes and subtropics is consistent with the general upward trend in Fig. 2. It means that as the surface warms, more longwave radiation is observed leaving the earth at the top of the atmosphere. Also, the negative sign
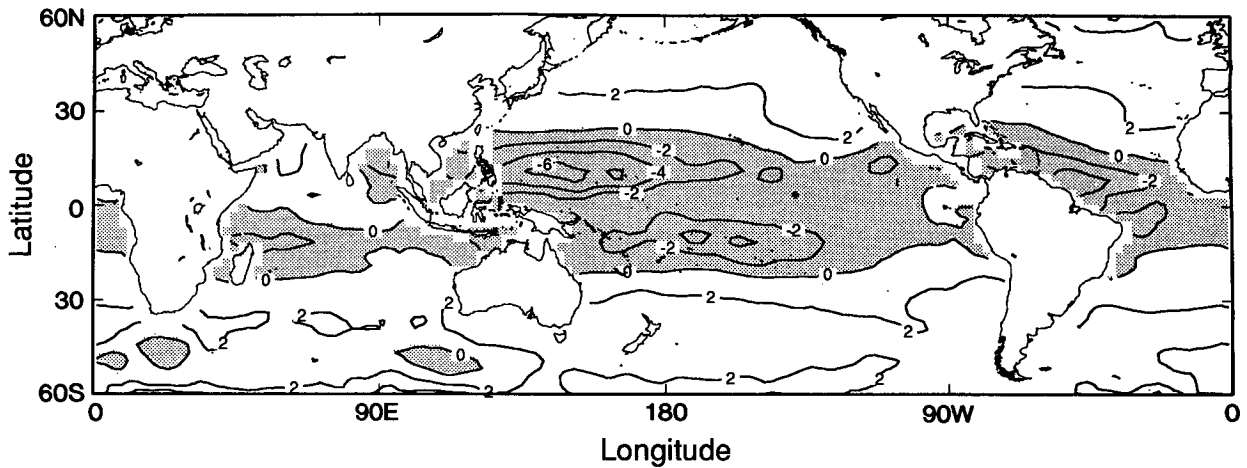
FIG. 3a. Global map of the slope of the clear-sky outgoing longwave radiation F_{cs} with respect to the sea surface temperature T_s (W m^{-2} K^{-1}), based on data from the period February 1985–December 1988. Areas with negative slope are shaded.

in the tropics is consistent with the highest temperature points in Fig. 2, and with the clear-sky slope map (Fig. 3a). The negative correlation is strongest at latitudes 10°–15° north and south. Deep convective clouds cannot account for a negative correlation between T_s and the clear-sky OLR (which is by definition cloud free). However, the humidity does increase drastically with temperature in the tropics, and this can have a distinct modulating effect on F_{cs} (Stephens 1990; Hallberg and Inamdar 1993).

Figure 4b shows the correlation between F_{cs} and W. Here again, r changes sign from the midlatitudes to the tropics. Although this plot differs in many details from Fig. 4a, its major features are broadly similar in showing regions of positive correlations poleward of 25° north and south, and negative correlations equatorward of the same latitudes. This suggests that although T_s and W affect F_{cs} in opposite directions, they are so closely correlated to each other that they give little independent information about the OLR.

Figure 4c shows the correlation between F_{cs} and $\overline{RH}$. Two features are apparent—first, the patterns of positive and negative correlations in midlatitudes bear little resemblance to those between F_{cs} and T_s (Fig. 4a). They seem instead to be more closely linked to the patterns of large-scale convection and subsidence. Second, large regions in the tropics show a negative correlation, in many areas with $r < -0.8$, which by most standards is considered highly significant (Spiegel 1961; Pan and Oort 1983). It appears that in the tropics F_{cs} is more consistently negatively correlated with $\overline{RH}$ than with either W or T_s. This is not surprising, since an increase in moisture that is uncorrelated to a change in T_s would generally lead to more longwave
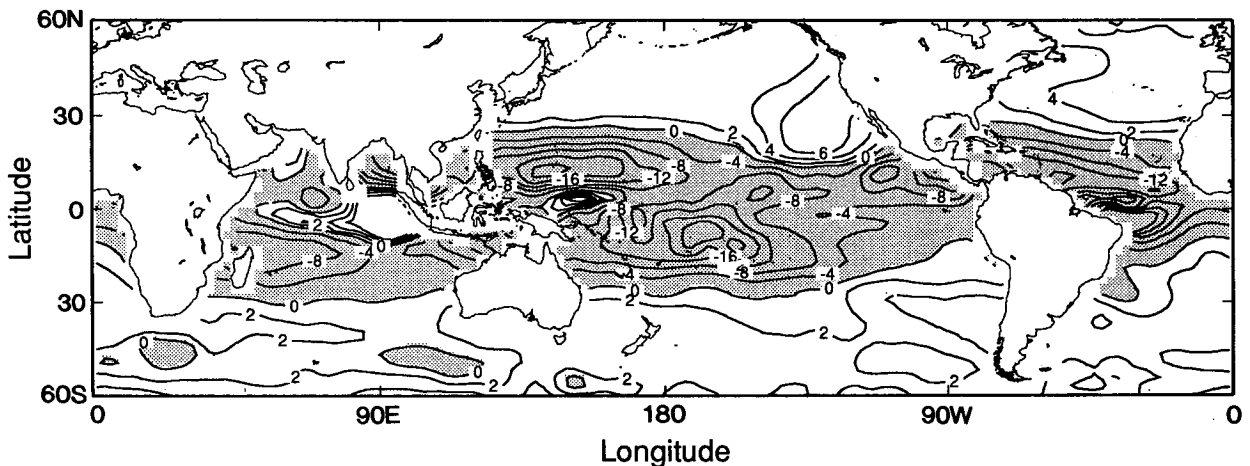

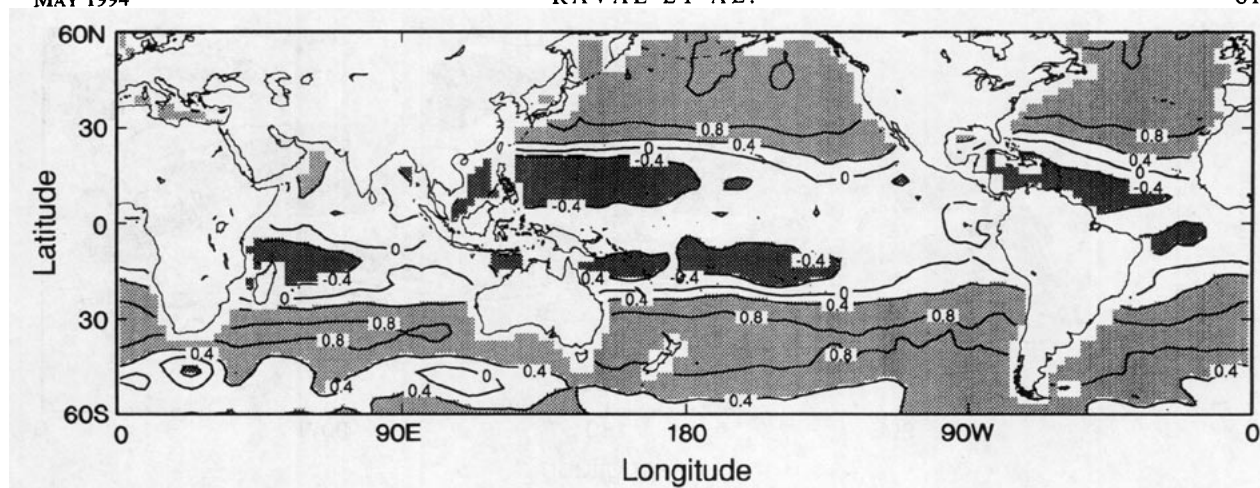FIG. 3b. Same as Fig. 3a except for total outgoing longwave radiation F_{tot}.

FIG. 4a. Global map of correlation of the clear-sky outgoing longwave radiation F_{cs} with respect to the sea surface temperature T_s, based on data from the period February 1985–December 1988. Heavy shading indicates areas with $r \leq -0.4$, light shading areas with $r \geq 0.4$. Values of $|r| \geq 0.4$ are estimated to be 95% significantly different from zero assuming 20 degrees of freedom.

trapping in the atmosphere and thus to a drop in the *OLR*.

Finally, we show correlations with F_{tot} and the same three climate variables in Figs. 4d, 4e, and 4f. It is very interesting to note that these figures exhibit similar patterns of negative and positive correlation to the F_{cs} figures but with a somewhat more complex structure. This greater complexity can be expected since the effects of clouds on the *OLR* are included in F_{tot}.

c. Correlation matrices

We can look at all the relationships discussed so far in a compact way by generating a set of correlation matrices for each geographical "region." Table 1 shows correlation matrices of the significant variables for the

following three noncontinuous latitude regions: 0°–15°S/°N, 15°–30°S/°N, and 30°–45°S/°N. Within each latitude belt, all the points for all 47 months are pooled together, and this pooled dataset is used to calculate the correlation matrix for that region. For example, the first section of Table 1, describing the inner tropics, deals with a geographical region that contains 1728 data grid points. Of these, roughly 75%, or 1290, are ocean points. The data over these ocean points, accumulated over 47 months, provide more than 50 000 samples that are then used to calculate the means, standard deviations, and the correlation matrix.

The regional correlations highlight the features presented previously in Fig. 4. For example, as we move from the midlatitudes to the subtropics and then to the inner tropics, the correlation between F_{cs} and W
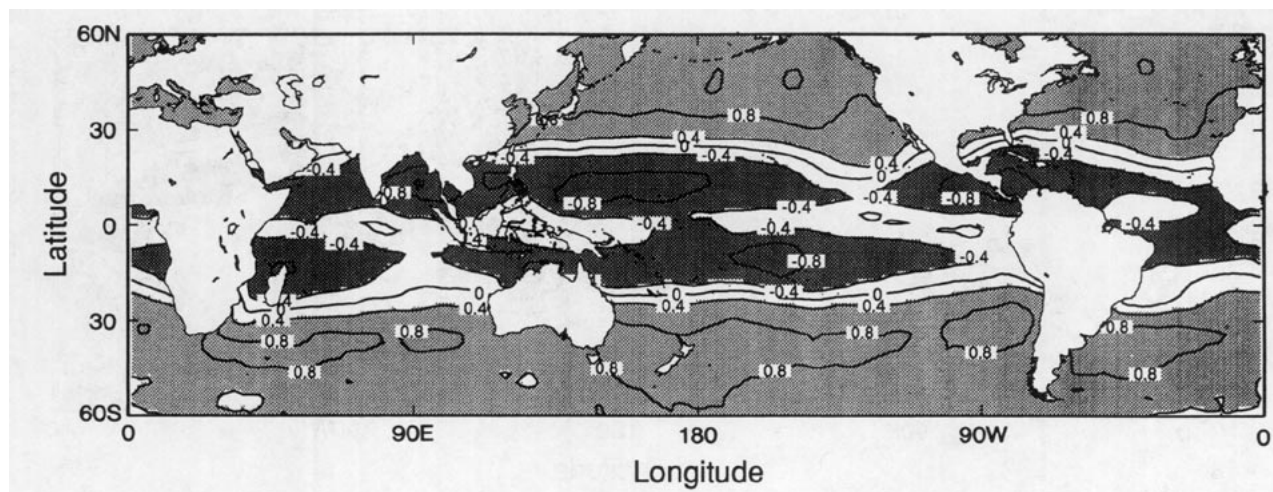

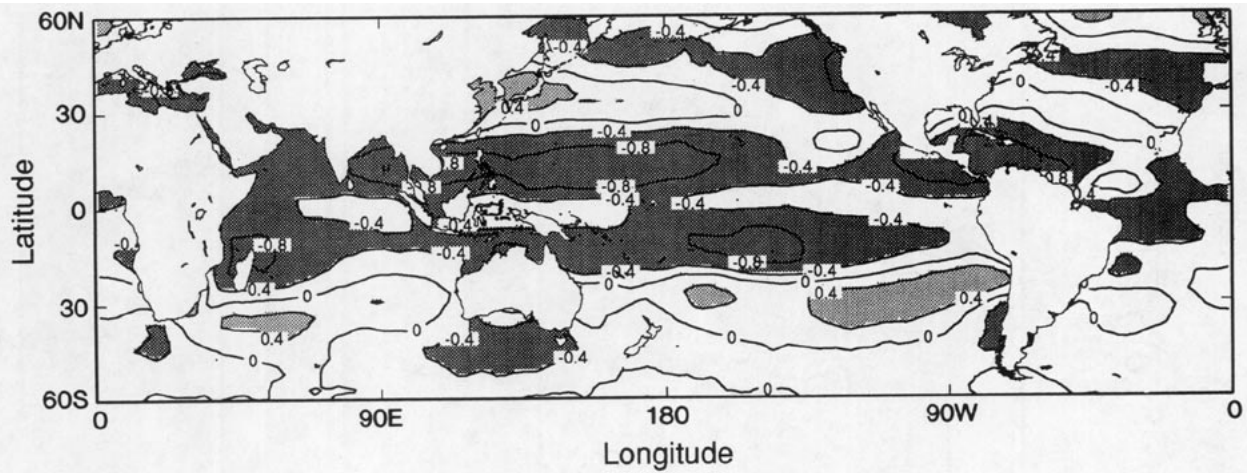FIG. 4b. Same as Fig. 4a except for correlation of F_{cs} with W.

FIG. 4c. Same as Fig. 4a except for correlation of F_{cs} with $\overline{RH}$.

changes from $+0.72$ to $+0.23$ to -0.58. Similar sign changes are found in the correlation between F_{tot} and W, and between either clear-sky or total OLR and T_s. In the midlatitudes, the correlation between F_{cs} and T_s is $r = +0.89$, which means that r^2, or 80%, of the variability of F_{cs} can be explained by surface temperature. Up to 45% of the variability of F_{tot} can be explained in similar fashion ($r = +0.68$). In the subtropics, however, the correlation between F_{tot} and T_s is zero, and between F_{cs} and T_s it is $r = +0.42$, which means that only about 20% of the variability of F_{cs} can be explained.

While these correlations all change sign from region to region, $r(F_{tot}, \overline{RH})$ remains at a relatively steady value of about -0.55. It is consistently negative in all three regions. Increasing relative humidity, in other words, always acts to reduce the OLR. Furthermore, correlations of T_s with $\overline{RH}$ are always less than cor-

relations of T_s with W. This shows the chief advantage of using $\overline{RH}$ as a measure of atmospheric humidity— it is not as strongly correlated with T_s, and thus is able to give more independent information about the OLR.

4. Two-parameter analysis

In this section, we apply a simple binning approach to untangle the multiple determinants on the OLR. It works not only when the input variables are relatively decoupled, as with T_s and $\overline{RH}$, but it also works when they are relatively strongly coupled, as with T_s and W. The binning approach relies on the fact that the covariation between the fields is never perfect. Field W, for example, does tend to increase as T_s increases, but by sampling many regions on the globe over several years, we would probably find instances where low W and high T_s coincide, and instances where high W and low T_s coincide.
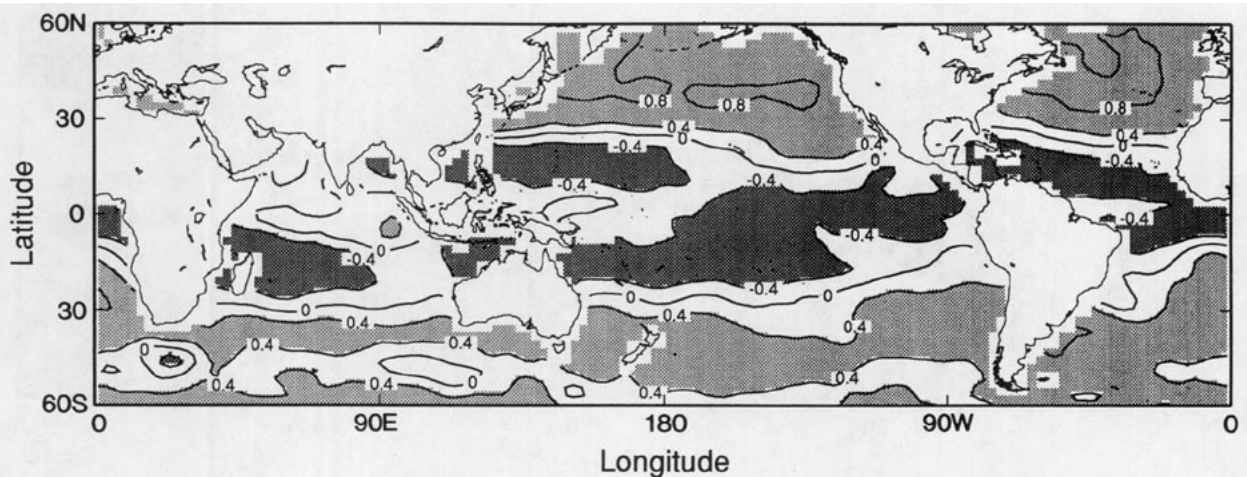

FIG. 4d. Same as Fig. 4a except for correlation of total outgoing longwave radiation F_{tot} with T_s.
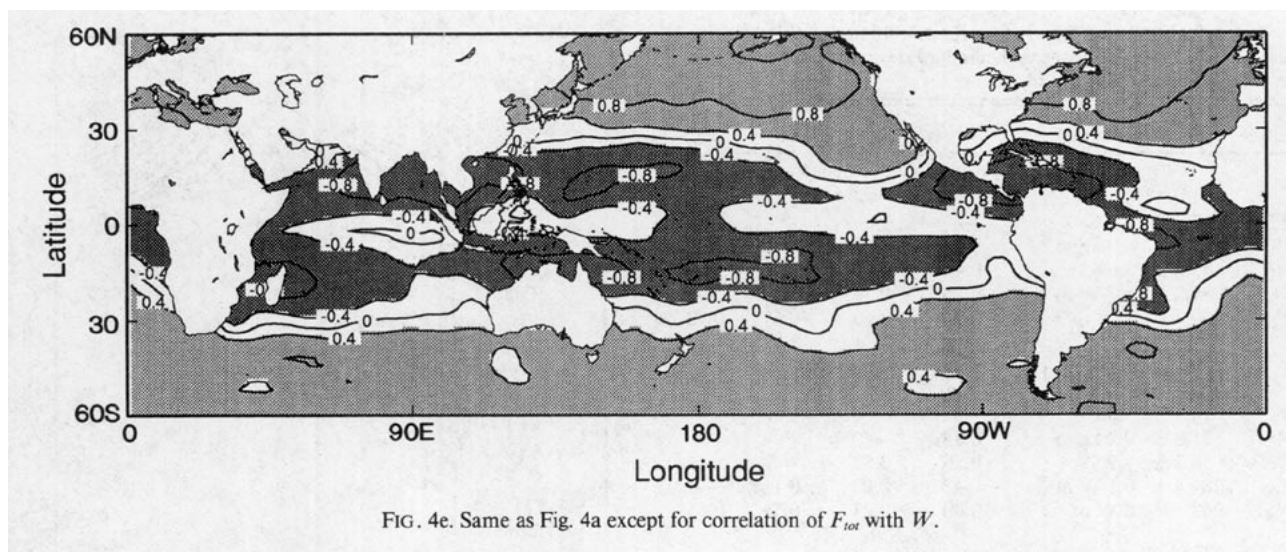
FIG. 4e. Same as Fig. 4a except for correlation of F_{tot} with W.

a. Binned ERBE phase-space portrait

The *OLR* is binned with respect to two parameters simultaneously to create a phase-space portrait. The portrait is derived by scanning through all the months in the dataset and all ocean regions that are between 60°S and 60°N and that are no farther than 2000 km from the nearest rawinsonde station. The distance criterion is designed to filter out points with the greatest chance of interpolation bias. To further control the quality of the portrait, only those bins that have accumulated more than 10 data points are retained. This has the slight effect of trimming the outer edges of the portrait.

The phase-space portraits in this section bin T_s by 2.5°C, W by 5 kg m^{-2}, and $\overline{RH}$ by 6%. On average, these bin sizes exceed the estimated uncertainties in each of these parameters. We can calculate not only

the mean value of the radiation flux at each bin, but also higher moments such as the standard deviation and the standard error of the mean.

1) BINNING WITH T_s AND W

Even though they are correlated, we can choose T_s and W as the two dimensions. Figure 5a shows the phase-space portrait for the ERBE clear-sky *OLR*, while Fig. 5b shows a representation of the ERBE total *OLR*.

In Fig. 5a, at low temperatures, below 10°C, F_{cs} primarily increases with W, but at higher temperatures, above 10°C, it mainly increases with T_s. For temperatures above 25°C and W greater than 40 kg m^{-2}, F_{cs} again varies primarily with W, but here the *OLR* decreases as the humidity rises. The real climate system generally moves along a phase-space path going diag-
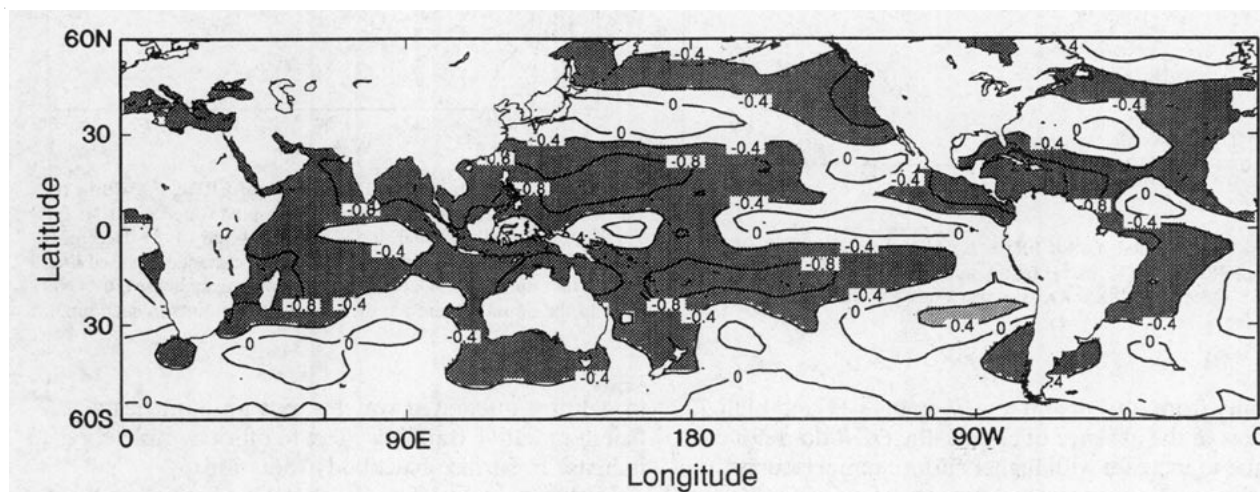

FIG. 4f. Same as Fig. 4a except for correlation of F_{tot} with $\overline{RH}$.

TABLE 1. Correlation tables of OLR and climate variables in three latitude regions. The means and standard deviations are calculated by the procedure described in section 3.

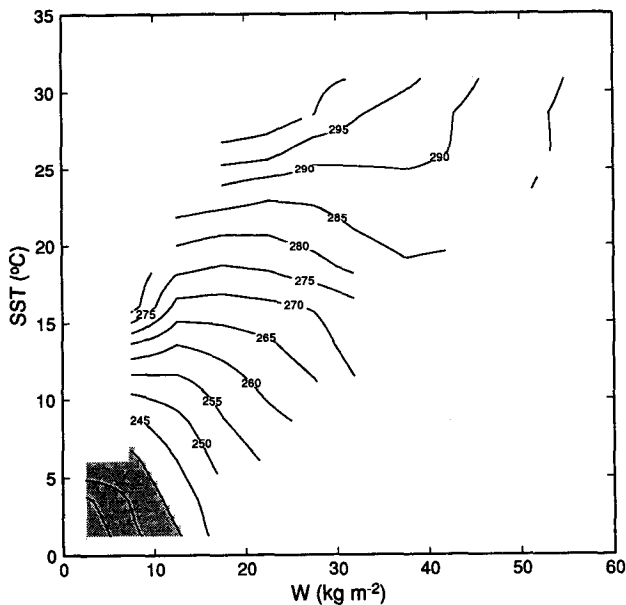|	Mean ± std der	T_s	W	RH	F_{cs}
	0°–15°S/°N				
T_s	27.7 ± 1.8 C	—			
W	45.2 ± 6.9 kg m⁻²	0.65	—		
RH	47.6 ± 8.6%	0.49	0.87	—	
F_{cs}	289.0 ± 5.7 W m⁻²	−0.29	−0.58	−0.63	—
F_{tot}	250 ± 27 W m⁻²	−0.51	−0.65	−0.67	0.72
	15°–30°S/°N				
T_s	24.4 ± 3.0 C	—			
W	31.8 ± 9.2 kg m⁻²	0.83	—		
RH	38.2 ± 7.9%	0.56	0.82	—	
F_{cs}	287.4 ± 6.1 W m⁻²	0.42	0.23	−0.15	—
F_{tot}	263 ± 18 W m⁻²	0.00	−0.23	−0.54	0.65
	30°–45°S/°N				
T_s	16.7 ± 4.5 C	—			
W	19.0 ± 6.1 kg m⁻²	0.79	—		
RH	39.6 ± 5.4%	−0.16	0.24	—	
F_{cs}	268 ± 11 W m⁻²	0.89	0.72	−0.31	—
F_{tot}	236 ± 20 W m⁻²	0.68	0.50	−0.49	0.80

FIG. 5a. Binned plot of ERBE F_{cs} with column-integrated water vapor W and T_s (W m⁻²), based on data from the period February 1985–December 1988. Areas with values less than 240 W m⁻² are shaded.

FIG. 5c. Plot of the standard deviation of ERBE F_{cs} within the various bins as a function of column-integrated water vapor W and T_s (W m⁻²), based on data from the period February 1985–December 1988. Areas with values less than 5 W m⁻² are shaded. Dashed lines of 10^2, 10^3, and 10^4 indicate the population density in the bins. Over most of the domain there are more than 1000 points in each bin.

onally from low W and low T_s to high W and high T_s. Thus, in the absence of clouds, the OLR does not continue to increase with higher surface temperatures (and correspondingly greater amounts of precipitable water), but reaches a peak value. At high T_s, the increase
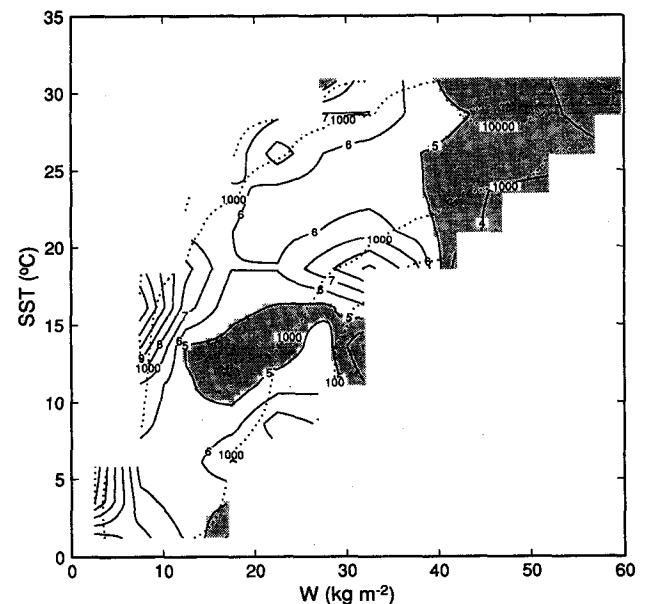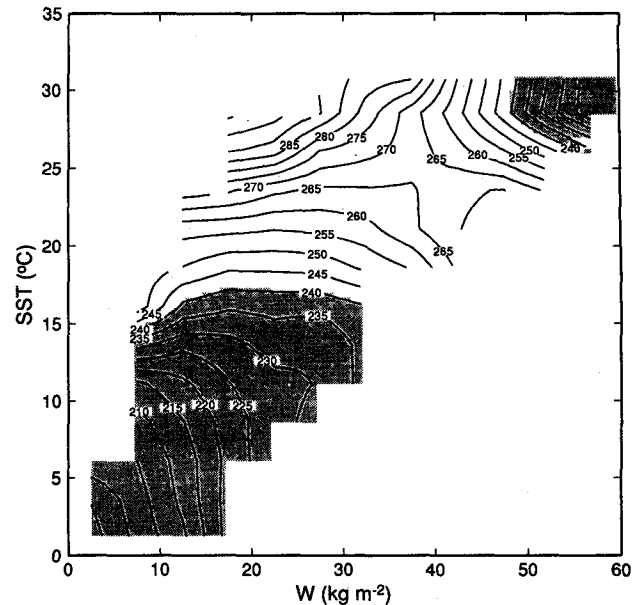
in column-integrated water vapor amount has a sufficient radiative trapping effect to offset completely the increase in surface blackbody radiation.

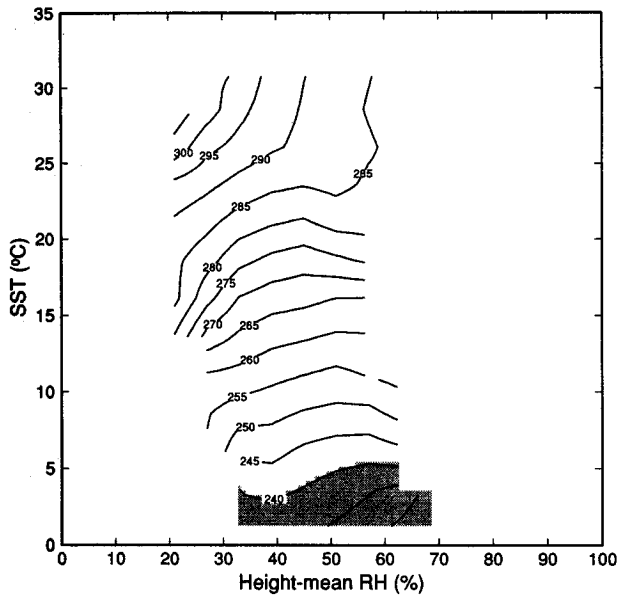Likewise, in Fig. 5b, F_{tot} shows a similar behavior, though it exhibits a much more dramatic drop for W

FIG. 6a. Binned plot of ERBE F_{cs} with height-mean $\overline{RH}$ and T_s (W m^{-2}), based on data from the period February 1985–December 1988. Areas with values less than 240 W m^{-2} are shaded.
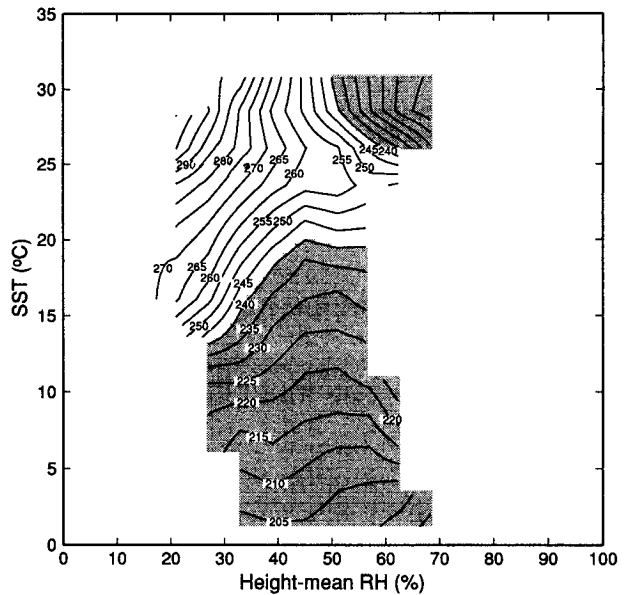

FIG. 6b. Same as Fig. 6a except for ERBE F_{tot}.

greater than 40 kg m^{-2}. Figure 5c shows the standard deviation (σ_{cs}) of the binned clear-sky OLR. Dotted lines are drawn to indicate the bins with a population of 100, 1000, and 10 000 data points. The population distribution indicates that within a large area of the plot, stray bad values will not significantly affect the binned values of F_{cs}. The standard deviations for those bins with 1000 or more data points range from about 4 to 8 W m^{-2}.

2) BINNING WITH T_s AND $\overline{RH}$

Figures 6a and 6b show the portraits of OLR with T_s and $\overline{RH}$, respectively, as the chosen dimensions. Because the last two variables are less tightly coupled, we obtain a phase space in which the data do not lie along the diagonal.

In both cases, the important features seem to be that at low temperatures (below about 10°–12°C) the OLR is not affected very much by the humidity, and instead varies chiefly with surface temperature. At higher temperatures, $\overline{RH}$ has a more and more important negative effect on the OLR. The change appears gradually with F_{cs}, while it appears much more abruptly with F_{tot}. Above 25°C, the contour lines in Figs. 6a and 6b become more nearly parallel to the T_s axis.

Because we will be comparing the binning of the ERBE clear-sky OLR with $\overline{RH}$ and T_s to radiative model results, it is important to ask at the outset how reliable the binned averages are. Figure 6c shows the standard deviation (σ_{cs}) of the binned clear-sky OLR.

As in Fig. 5c, the dotted lines in Fig. 6c indicate the bins with a population of 100, 1000, and 10 000 points. Similarly, as in Fig. 5c, the standard deviations within the area enclosed by the 1000-count dotted line ranges from 4 to 8 W m^{-2}.

Below 14°C, the range in values of F_{cs} at a given T_s across the full range of $\overline{RH}$ is less than the binned σ_{cs}
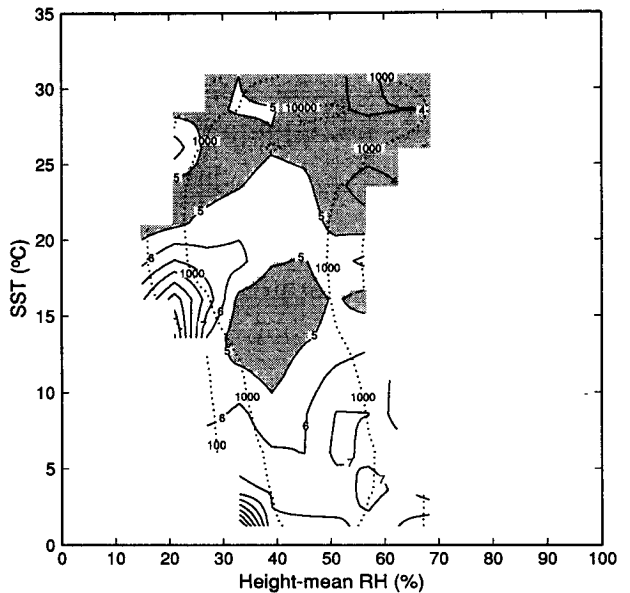

FIG. 6c. Plot of the standard deviation of ERBE F_{cs} within the various bins as a function of height-mean $\overline{RH}$ and T_s (W m^{-2}). See caption of Fig. 5c for more information.

for that same T_s (compare Figs. 6a and 6c). For example, at $T_s = 8.75°C$, F_{cs} varies from 247 to 253 W m^{-2}, a range of 6 W m^{-2}, while the individual σ_{cs} hover around 7 W m^{-2}. Thus, at this temperature, F_{cs} does not statistically differentiate between 30% and 70% height-mean relative humidity. Because the saturation pressure is so low, even a 40% variation in $\overline{RH}$ does not amount to a radiatively significant change in the total precipitable water. Above 14°C, however, F_{cs} does differentiate along the range of values of $\overline{RH}$. For example, at $T_s = 25.25°C$, F_{cs} has a range of 22 W m^{-2}, while σ_{cs} has a mean value of 5 W m^{-2}. Clearly, in this temperature regime, observed differences in $\overline{RH}$ for points that have the same T_s do lead to measurable differences in the binned OLR.

b. Radiative model results

Thompson and Warren (1982) fit the results of a detailed radiative transfer model to a third-order polynomial in T_s whose coefficients are second-order polynomials in $\overline{RH}$. The detailed model is based on Wiscombe's *exponential sum fitting of transmission functions* method (Wiscombe and Evans 1977). Thompson and Warren consider both total OLR and clear-sky OLR cases in their paper. Here, we display the clear-sky phase-space portrait derived directly from Thompson and Warren's polynomial model, with their coefficients. The main reasons for choosing this model are (a) its simplicity, and (b) its use of height-mean relative humidity as a parameter in deriving the OLR. As de-
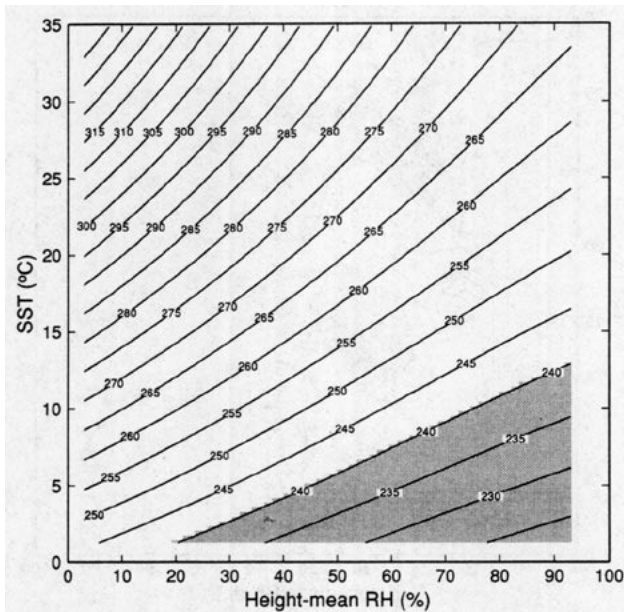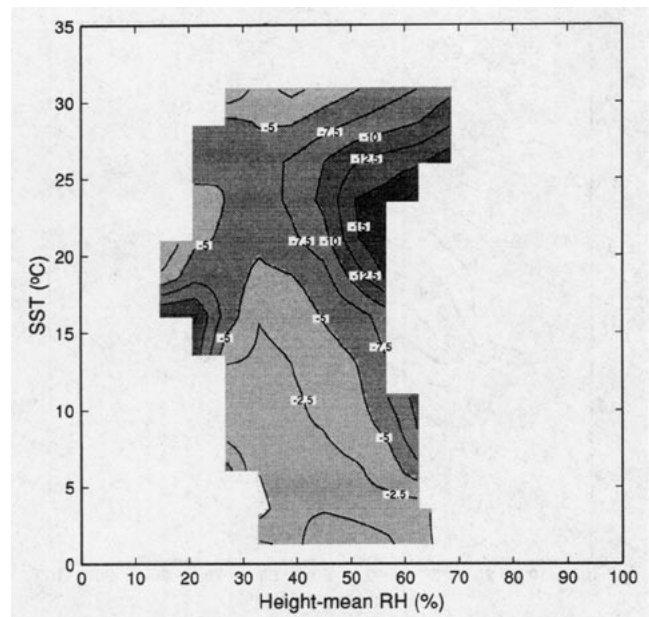

FIG. 7b. Binned plot of difference of polynomial fit model for F_{cs} (Thompson and Warren 1982) minus ERBE F_{cs}, with height-mean $\overline{RH}$ and T_s (W m^{-2}).

scribed in section 2, Thompson and Warren explicitly choose $\overline{RH}$ as a parameter in the polynomial fit because they find that the OLR is not significantly affected by vertically redistributing the moisture while holding $\overline{RH}$ fixed. In their detailed radiative transfer calculation, they maintain a constant temperature profile as they redistribute the moisture. In the present study, when we compare observed OLR binned with respect to T_s and $\overline{RH}$ with model OLR, we have not ensured that the temperature profiles are necessarily the same in both cases.

Figure 7a shows the portrait resulting from the Thompson–Warren model. As one would expect for a polynomial expression, F_{cs} varies smoothly over the whole space, but it preferentially shows a larger gradient with respect to T_s at low temperatures (midlatitudes), and a larger gradient with respect to $\overline{RH}$ at high temperatures (tropics). Thus, as one moves from colder to warmer climates, the relative humidity becomes a progressively more important factor in determining the OLR.

Figure 7b shows the difference between the radiative model calculations of F_{cs} and the ERBE data. The plot is negative throughout most of the phase space, with a mean discrepancy of around 7–8 W m^{-2}, and extreme values around 18 W m^{-2}, indicating that the radiative model predicts lower values of F_{cs} than the ERBE observations. Thompson and Warren indicate that their curve fits are generally within a few watts per square meter of the results from their detailed radiative model, with a maximum error of 10 W m^{-2}. Their detailed

FIG. 7a. Binned plot of polynomial fit model F_{cs} with height-mean $\overline{RH}$ and T_s (W m^{-2}). Areas with values less than 240 W m^{-2} are shaded.

reference model could itself have uncertainties in the *OLR* of about ±2% (about 5–6 W m^{-2}), relative to line-by-line results (Ellingson et al. 1991). Furthermore, the curve fits do not account for the effects of non–CO_2 trace gases (methane, nitrous oxide, and CFCs), which would contribute to a further lowering of the model clear-sky OLR of up to ~5 W m^{-2} (Slingo and Webb 1992).

One can also compare this mean discrepancy in Fig. 7b with the estimated 3–4 W m^{-2} positive bias in the ERBE clear-sky *OLR* results (Harrison et al. 1990; Slingo and Webb 1992). Thus, the discrepancies may be caused partly by errors in the observed *OLR*, partly by errors introduced by the simplistic assumptions of the Thompson and Warren polynomial model, and partly by errors associated with the detailed radiative model, including uncertainties in actual vertical profiles of temperature and moisture. While the precise reasons for the discrepancy corresponding to a particular $\overline{RH}$–T_s combination could involve all of the above-mentioned factors, Fig. 7 does illustrate how observed data and specific model results may be usefully compared.

c. General circulation model results

We compare the ERBE clear-sky *OLR* with the *OLR* obtained from a radiative transfer model incorporated in the Geophysical Fluid Dynamics Laboratory (GFDL) global R15 general circulation model (GCM). The GCM is described in Wetherald et al. (1991). The model is semispectral, rhomboidally truncated at wavenumber 15 and has nine vertical finite-difference levels. The simulations use the annual cycle of insolation and the observed climatological T_s. The continuity equation for water vapor is solved prognostically. The model is first run to equilibrium, and a subsequent 10-yr simulation is analyzed.

In the GCM, the height-mean relative humidity is evaluated using the nine vertical levels of data. The clear-sky *OLR* at a grid point is defined as the mean of the values accumulated over the 10-yr simulation for which there are no clouds in any of the layers at that point.

Figure 8a shows a phase-space plot of the 10-yr mean GCM results. Comparing this figure with Fig. 6a, it appears that the model's phase space is narrower, especially along the $\overline{RH}$ axis, than that generated from observations. Also, the $\overline{RH}$ values in the model tend to be slightly higher overall. In the model, the effect of relative humidity on the *OLR* is apparent only at the higher surface temperatures (above about 10°C).

Figure 8b shows the differences with respect to the ERBE observations. For similar T_s and relative humidity conditions, the GCM tends to yield more *OLR*; that is, the model has a lower clear-sky greenhouse effect than the observations. The *OLR* bias attains val-
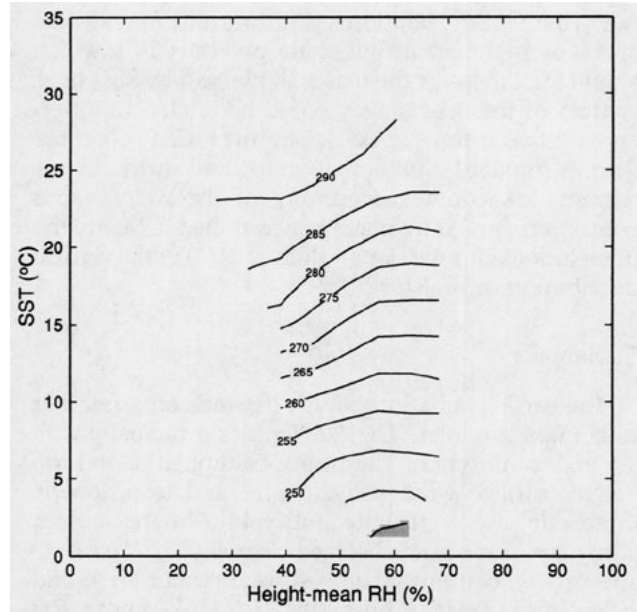

FIG. 8a. Binned plot of GFDL R15 model F_{cs} with height-mean $\overline{RH}$ and T_s based on 10 model years (W m^{-2}).

ues of up to 10 W m^{-2}. As noted in Wetherald et al. (1991), the moisture field of the GCM may be inadequately simulated. Other GCMs, too, exhibit this feature in the clear-sky regions (Kiehl and Ramanathan 1990). From Fels et al. (1991), the radiation algorithm used in this GCM (including effects of H_2O, CO_2, O_3) underestimates the clear-sky *OLR* by about 2 W m^{-2}.
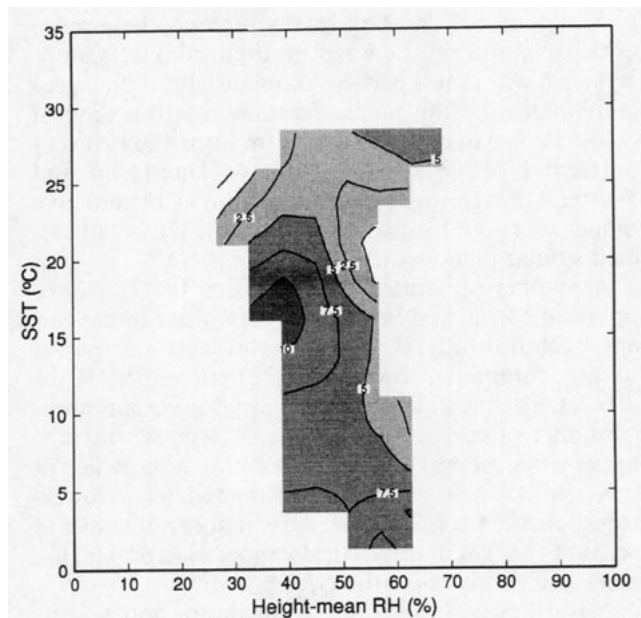

FIG. 8b. Binned plot of difference of GFDL R15 model F_{cs} minus ERBE F_{cs}, with height-mean $\overline{RH}$ and T_s (W m^{-2}).

Also, the GCM radiation code does not include the effects of methane, nitrous oxide, and the CFCs, which would tend to lower the biases shown in Fig. 8b. Other sources of the discrepancy could be related to differences between the values of T_s in the GCM (obtained from a standard climatology map) and in the observations, inadequate accounting of the water vapor continuum, and differences between the GCM and the observations (for the same values of $\overline{RH}$) in the vertical distribution of moisture.

5. Summary

The earth's radiation budget depends on a number of climate variables. The OLR varies principally with T_s and atmospheric humidity, although cloud-top height, surface wind convergence, and tropospheric lapse rate also contribute noticeably. In the present study, we binned the observed clear-sky OLR with respect to T_s, column-integrated water vapor (W), and height-mean relative humidity ($\overline{RH}$). We chose $\overline{RH}$ to represent atmospheric humidity because in Thompson and Warren's study (1982) the OLR was found to be approximately invariant to changes in the vertical relative humidity profile that do not alter the height-weighted mean. The phase-space portraits resulting from the binning indicate that T_s drives the OLR in the midlatitudes, while T_s and $\overline{RH}$ together drive it in the subtropics and tropics.

A reasonably accurate climate model should adhere not only to the observed mean climate state, but also to the observed functional dependence of the OLR on basic climate parameters. The phase-space portrait illustrates one means by which models can be compared against observed data. It visually presents the essence of the relationships between multiple climate parameters in a way that is perhaps more insightful than geographic distribution maps. To show that this kind of comparison can be made easily, we turned to two very different types of climate models—Thompson and Warren's simple third-order polynomial fit radiative model, and an R15 spectral GCM at GFDL—and created similar phase-space portraits of them.

A number of parameters that affect the OLR have not been considered in this study. In order to use this approach fruitfully, it will be important to design humidity parameters more robust than either W or $\overline{RH}$. Height-mean relative humidity has certain problems that other parameters do not. It is sensitive to upper-tropospheric humidity measurements, which at this point are neither as accurate nor as dense as lower-tropospheric measurements. Also, it does not take into account changes in the vertical temperature profile that can significantly affect the OLR.

Nevertheless, the surface temperature and height-mean relative humidity together do explain a substantial amount of the variation in the observed clear-sky

OLR; a different humidity variable or an additional independent variable, such as the lapse rate, could make the analysis even more realistic. As a potentially useful extension of the two-dimensional binning, one could create a series of portraits, each of which restricts a third variable to a different range of values.

REFERENCES

Barkstrom, B., 1984: The earth radiation budget experiment (ERBE). *Bull. Amer. Meteor. Soc.,* **65,** 1170–1185.

——, E. Harrison, G. Smith, R. Green, J. Kibler, R. Cess, and the ERBE Science Team, 1989: Earth Radiation Budget Experiment (ERBE) archival and April 1985 results. *Bull. Amer. Meteor. Soc.,* **70,** 1254–1262.

Budyko, M. I., 1968: On the origin of ice ages. *Meteor. Gidrol.,* **11,** 3–12.

——, 1969: The effect of solar radiation variations on the climate of the earth. *Tellus,* **21,** 611–619.

Cess, R. D., 1976: Climate change: An appraisal of atmospheric feedback mechanisms employing zonal climatology. *J. Atmos. Sci.,* **33,** 1831–1843.

Ellingson, R. G., J. Ellis, and S. B. Fels, 1991: The intercomparison of radiation codes used in climate models: Longwave results. *J. Geophys. Res.,* **96,** 8929–8953.

Fels, S. B., J. T. Kiehl, A. A. Lacis, and M. D. Schwarzkopf, 1991: Infrared cooling rate calculations in operational general circulation models: Comparisons with benchmark computations. *J. Geophys. Res.,* **96,** 9105–9120.

Graham, N. E., and T. P. Barnett, 1987: Sea surface temperature, surface wind divergence, and convection over tropical oceans. *Science,* **238,** 657–659.

Greenwald, T. J., G. L. Stephens, T. H. Vonder Haar, and D. L. Jackson, 1993: A physical retrieval of cloud liquid water over the global oceans using SSM/I observations. *J. Geophys. Res.,* **98,** 18 471–18 488.

Gutzler, D. S., and T. M. Wood, 1990: Structure of large-scale convective anomalies over tropical oceans. *J. Climate,* **3,** 483–496.

Hallberg, R., and A. K. Inamdar, 1993: Observations of seasonal variations in atmospheric greenhouse trapping and its enhancement at high sea surface temperature. *J. Climate,* **6,** 920–931.

Harrison, E. F., P. Minnis, B. R. Barkstrom, V. Ramanathan, R. D. Cess, and G. G. Gibson, 1990: Seasonal variation of cloud radiative forcing derived from the Earth radiation budget experiment. *J. Geophys. Res.,* **95,** 18 687–18 703.

Kiehl, J. T., and V. Ramanathan, 1990: Comparison of cloud forcing derived from the Earth Radiation Budget Experiment with that simulated by the NCAR Community Climate Model. *J. Geophys. Res.,* **95,** 11 679–11 698.

Kubota, I., 1989: Land-sea differences of the earth radiation budget. *Geophys. Mag.,* **43,** 19–43.

North, G. R., R. F. Cahalan, and J. A. Coakley, 1981: Energy balance climate models. *Rev. Geophys. Space Phys.,* **19,** 91–121.

Oort, A. H., 1983: Global atmospheric circulation statistics. 1958–1973, *Professional Paper 14,* National Oceanic and Atmospheric Administration, Rockville, MD. [Available from GFDL/NOAA, P.O. Box 308, Princeton, NJ 08542.]

Pan, Y.-H., and A. H. Oort, 1983: Global climate variations connected with sea surface temperature anomalies in the eastern equatorial Pacific Ocean for the 1958–1973 period. *Mon. Wea. Rev.,* **111,** 1244–1258.

Ramanathan, V., R. D. Cess, E. F. Harrison, P. Minnis, B. R. Barkstrom, E. Ahmad, and D. Hartmann, 1989: Cloud-radiative forcing and climate: Results from the earth radiation budget experiment. *Science,* **243,** 57–62.

Raval, A., and V. Ramanathan, 1989: Observational determination of the greenhouse effect. *Nature,* **342,** 758–761.

Sellers, W. D., 1969: A climate model based on the energy balance of the earth–atmosphere system. *J. Appl. Meteor.,* **8,** 392–400.

Short, D. A., G. R. North, T. D. Bess, and G. L. Smith, 1984: Infrared parameterization and simple climate models. *J. Climate Appl. Meteor.,* **23,** 1222–1233.

Slingo, A., and M. Webb, 1992: Simulation of clear-sky outgoing longwave radiation over the oceans using operational analyses. *Quart. J. Roy. Meteor. Soc.,* **118,** 1117–1144.

Spiegel, M. R., 1961: *Statistics. Schaum's Outline Series in Mathematics,* McGraw Hill, 359 pp.

Stephens, G. L., 1990: On the relationship between water vapor over the oceans and sea surface temperature. *J. Climate,* **3,** 634–645.

——, D. A. Randall, I. L. Wittmeyer, and D. A. Dazlich, 1993: The earth's radiation budget and its relation to atmospheric hydrology. 3. Comparison of observations over the oceans with a GCM. *J. Geophys. Res.,* **98**(D3), 4931–4950.

Stephenson-Graves, D., 1982: A comparison between satellite-defined and parameterized land-water differences in emitted longwave radiation. *J. Atmos. Sci.,* **39,** 1163–1170.

Thompson, S. L., and S. G. Warren, 1982: Parameterization of outgoing infrared radiation derived from detailed radiation calculations. *J. Atmos. Sci.,* **39,** 2667–2680.

Warren, S. G., and S. H. Schneider, 1979: Seasonal simulation as test for uncertainties in the parameterization of a Budyko-Sellers zonal climate model. *J. Atmos. Sci.,* **36,** 1377–1391.

——, and S. L. Thompson, 1983: The climatological minimum in tropical outgoing infrared radiation: Contributions of humidity and clouds. *Quart. J. Roy. Meteor. Soc.,* **109,** 169–185.

Wetherald, R. T., V. Ramaswamy, and S. Manabe, 1991: A comparative study of the observations of high clouds and simulations by an atmospheric general circulation model. *Climate Dyn.,* **5,** 135–143.

Wiscombe, W. J., and J. W. Evans, 1977: Exponential-sum fitting of radiative transmission functions. *J. Comput. Phys.,* **24,** 416–444.